Experimental evidence of early-time saturation of the ion-Weibel instability in counterstreaming plasmas of CH, Al, and Cu

M. J.-E. Manuel [1,*] M. B. P. Adams [2] S. Ghosh,[3] F. N. Beg,[3] S. Bolaños,[3] C. M. Huntington,[4] R. Jonnalagadda,[3]
D. Kawahito,[3] B. B. Pollock,[4] B. A. Remington,[4] J. S. Ross,[4] D. D. Ryutov,[4] H. Sio,[4] G. F. Swadling [4]
P. Tzeferacos,[2] and H.-S. Park [4]

[1]*General Atomics, San Diego, California 92121, USA*
[2]*University of Rochester, Rochester, New York 14627, USA*
[3]*University of California San Diego, San Diego, California 92093, USA*
[4]*Lawrence Livermore National Laboratory, Livermore, California 94450, USA*

The collisionless ion-Weibel instability is a leading candidate mechanism for the formation of collisionless shocks in many astrophysical systems, where the typical distance between particle collisions is much larger than the system size. Multiple laboratory experiments aimed at studying this process utilize laser-driven ($I \gtrsim 10^{15}$ W/cm^2), counterstreaming plasma flows ($V \lesssim 2000$ km/s) to create conditions unstable to Weibel-filamentation and growth. This technique intrinsically produces temporally varying plasma conditions at the midplane of the interaction where Weibel-driven B fields are generated and studied. Experiments discussed herein demonstrate robust formation of Weibel-driven B fields under multiple plasma conditions using CH, Al, and Cu plasmas. Linear theory based on benchmarked radiation-hydrodynamic FLASH calculations is compared with Fourier analyses of proton images taken ∼5–6 linear growth times into the evolution. The new analyses presented here indicate that the low-density, high-velocity plasma-conditions present during the first linear-growth time (∼300–500 ps) sets the spectral characteristics of Weibel filaments during the entire evolution. It is shown that the dominant wavelength (∼300 μm) at saturation persists well into the nonlinear phase, consistent with theory under these experimental conditions. However, estimates of B-field strength, while difficult to determine accurately due to the path-integrated nature of proton imaging, are shown to be in the ∼10–30 T range, an order of magnitude above the expected saturation limit in homogenous plamas but consistent with enhanced B fields in the midplane due to temporally varying plasma conditions in experiments.

I. INTRODUCTION

Collisionless shocks are ubiquitous in astrophysics and a possible source of the highest-energy cosmic rays in our universe [1–5]. Telescopic observations of astrophysical systems, such as supernova remnants (SNRs) and pulsar wind nebulae, show well-formed shocks even though the mean free path (λ_{mfp}) between particles is much larger than the observed shock size. Typical (collisional) shocks are formed when the particle velocity (V) is faster than the speed of pressure waves, mediated by particle collisions. Hence, the thickness of these shocks is only a few mean free paths wide, where $\lambda_{\mathrm{mfp}} = V\tau$ and τ is the typical time between collisions. In emitting astrophysical SNRs, particle densities are often of order $n \sim 1$ cm^{-3}, temperatures are $T \sim 1$ eV, and particle velocities are $V \sim 2000$ km/s, such that $\lambda_{\mathrm{mfp}} \sim 30$ ly for ions, much longer than the system size. However, shocks are observed in these "collisionless" systems, where the presence and amplification of electromagnetic fields have been observed [6]. These field structures are proposed as the mechanism by which collision-

less shocks may form and where high-energy cosmic rays are generated.

The Weibel instability [7,8] is a leading candidate mechanism for the formation and amplification of B fields to the levels responsible for mediating collisionless shocks in astrophysical systems [5,9] as well as present explanations for B fields in cosmic voids [10]. Weibel is a kinetic instability that arises due to anisotropy in the particle-velocity distribution function and can be driven by both electrons and ions. The collisionless Weibel instability can be triggered when two counterstreaming plasmas interact with relative velocity V, e.g., supernova-ejecta passing through the interstellar medium. This instability causes current-density perturbations to grow and filament, thereby generating filamentary B-field structures. During the linear phase, perturbations grow exponentially, where the nonrelativistic, characteristic growth rate (γ_W) and size (λ_W) for the ion-Weibel instability scale as

$$\gamma_W \sim \frac{V}{\delta_{pi}}, \qquad (1)$$

$$\lambda_W \sim \delta_i, \qquad (2)$$

where ($\delta_i = c/\omega_{pi}$) is the ion skin-depth, c is the speed of light, and $\omega_{pi} \propto \sqrt{n_i Z^2/m_i}$ is the ion plasma frequency, that

depends on the ion charge state Z, mass m_i, and number density n_i. Early in the evolution, the electron-Weibel instability may occur, though on shorter temporal and spatial scales than the ion-Weibel instability. During the linear-growth phase, current-density filaments remain roughly constant in size, but the amplitude of the current increases, resulting in exponential growth of the azimuthal magnetic fields surrounding them. Once the fields are strong enough, they provide a stabilizing mechanism through magnetic trapping to reach a saturation value B_{tr}. This limit is reached when the ion displacement due to the quiver-motion in the B field approaches the unstable wavelength [11–14]

$$B_{tr} \sim \frac{m_i \Gamma^2(k)}{q_i k V}, \tag{3}$$

where $\Gamma(k)$ is the linear growth rate at mode k, and q_i is the ion charge. For the most unstable modes, the wavelengths are near the ion skin depth, and the resulting field strength associated with the most unstable modes simply scale as

$$B_{tr,W} \sim V\sqrt{m_i n_i}, \tag{4}$$

After saturation, nonlinear growth and filament merging occurs [15], increasing the size of the filaments, but leaving the B-field strength roughly constant for homogenous, constant plasma conditions. Eventually longitudinal modes become important, and the fields evolve into a turbulent state that can mediate shock formation and amplify background B fields.

In the past decade, there has been significant interest in studying formation of collisionless shocks in the laboratory [16–27]. The experimental platform of interest to this work involves the interpenetration of two opposing plasma flows, wherein the overlapped region of the two ion streams is collisionless, though the electrons are collisional [17]. These laboratory systems are relevant for high Mach-number shocks, from fully unmagnetized to weakly magnetized regimes in which the Weibel instability still develops at the shock front. Previous works utilizing this platform have demonstrated formation of Weibel filamentation through visualization of filamentary B-field structures using proton imaging [18,20,21,28] and through direct measurement of current filaments inferred from Thomson-scattering data [25]. Recently, electron acceleration has also been observed [27] in collisionless shock experiments at the National Ignition Facility. The majority of previously published works utilizing this platform implement low-Z foils, such as plastic (CH) or beryllium, to drive ion-Weibel filamentation in the interaction region of the experiment. The work presented here complements previous studies by studying Weibel-filamentation in plastic, aluminum, and copper plasmas. The new analysis techniques presented herein experimentally demonstrate that the plasma conditions in the overlapped region present during the first linear growth-time ($\sim$300–500 ps) of the interaction set the spectral evolution of ion-Weibel filaments under varying plasma conditions and across ion species. These experimental results are consistent with recent computational work [29] that showed similar spectral characteristics through the nonlinear-growth phase between homogenous and inhomogenous plasma conditions, though B-field strengths were

shown to continuously increase after saturation when the plasma density increased in time.

II. EXPERIMENTAL RESULTS

Experiments to study Weibel-filament generation under varying plasma parameters were conducted on the Omega laser system [30]. The general configuration is shown in Fig. 1(a), whereby two disks of the same material (plastic, aluminum, or copper) are set opposite each other by 5 or 8 mm. Two sets of Omega beams ($\lambda = 0.351$ μm) drive the two targets in a $\sim$300 μm spot with $\sim$3300 J (8 mm separation) or $\sim$2800 J (5 mm separation) in a 1 ns square pulse ($I \sim 4 \times 10^{15}$ W/cm^2). The hot plasma plumes supersonically expand from the surface and meet in the midplane of the experiment [21]. The system is characterized by two primary diagnostics: optical Thomson scattering (TS) and proton imaging.

Weibel filamentation is visualized using monoenergetic proton imaging [28,31], as shown in Fig. 1(b). The proton imaging technique utilizes a D^{3}He-filled capsule ($\sim$400 μm diameter) placed 1cm from the midplane, in a direction perpendicular to the flow axis. A separate set of laser beams implodes the capsule after the opposing plasma flows reach the midplane. A quasiuniform flux of monoenergetic ($\sim$15 MeV) fusion protons with a $\sim$45 μm full-width-half-max (FWHM) source-size is created during the implosion. Protons traverse the interaction region (at $\sim$3.5 and $\sim$4.5 ns for the 5 and 8 mm cases, respectively) and are deflected by electromagnetic fields in the plasma, then recorded on a CR39 detector 30 cm from the source (magnification $M = 30$). Coulomb scattering within the low-density plasma is negligible, such that deviations from unity in normalized proton-fluence images may be attributed to electromagnetic fields. Divergence of the proton beam allows for sensitivity to the locally azimuthal B fields around current filaments generated by the ion-Weibel instability that are primarily aligned with the flow axis. Asymmetric vertical deflections in Fig. 1(b) are likely caused by advected field structures from the laser-target interaction, which have a minimal effect on the evolution of the Weibel instability above and below the midplane [32]. As protons traverse the field of Weibel filaments, deflections in their trajectory encode the path-integrated B-field strength. In this proton-imaging geometry, the so-called "forest-effect" [18] of the path-integrated B-field measurement can be used to characterize the size of the Weibel filaments through Fourier analysis in the linear deflection regime; for the work presented, this is true when $B \lesssim 50$ T [33].

Plasma conditions at the midplane are characterized using temporally resolved collective Thomson scattering (TS) [17]. A summary of the plasma conditions, electron density (n_e) and electron temperature (T_e), from the six different cases are shown in Fig. 1(c), where the error bars indicate variation of the inferred parameters over the probe beam duration. A 1 ns square pulse containing 40 J of 0.527 μm light is focused to a $\sim$70 μm spot in the center of the midplane. Thomson-scattered light is collected by an f/10 optic, spectrally dispersed, and temporally resolved on a streak camera. The scattering volume can be approximated by a $\sim$10^{-3} mm^3
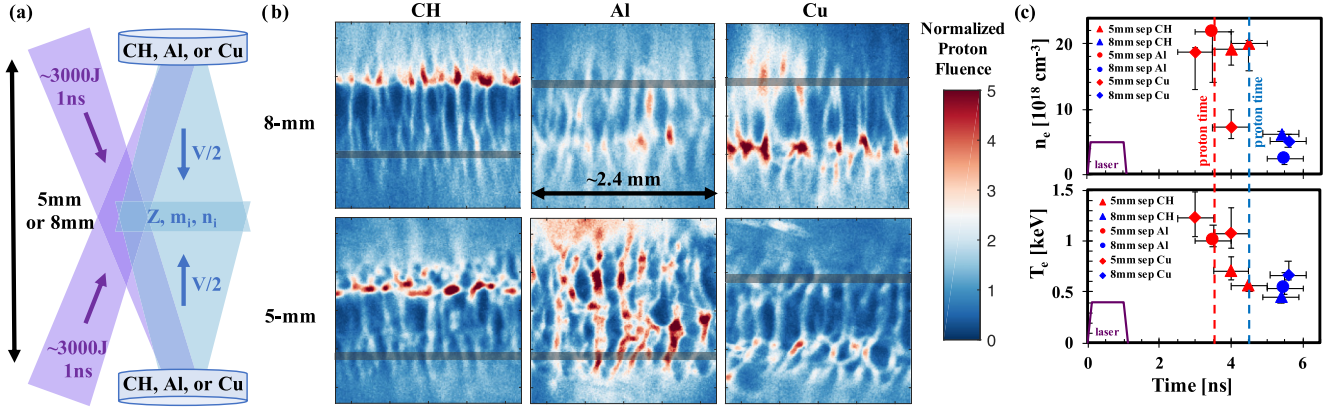
FIG. 1. (a) Laser-irradiated solid foils generate supersonic plasma plumes that interact at the mid-plane of the experiment. (b) Normalized proton fluence images of the six experimental cases; plastic (CH), aluminum (Al), or copper (Cu) at a 5 or 8 mm separation distance. All images are on the same color scale and show filamentary structures in proton fluence created by deflections due to Weibel-driven magnetic fields. The overlaid boxes indicate the region of analysis away from the large horizontal voids in proton fluence. (c) Summary of Thomson scattering measurements for all six cases. Error bars show variation over the 1 ns probe time, not uncertainty in the measurement. The laser pulse and proton arrival times are shown for reference.

volume at target-chamber-center (TCC). TS measurements were taken at ∼2.5–5 and ∼5–6 ns for the 5 and 8 mm cases, respectively. While ions are collisionless between the two plasma flows at the midplane ($\lambda_{\mathrm{mfp}} \gtrsim 100$ mm), the electrons are collisional and quickly isotropize their flow velocity to thermal energy [34], as previously observed in experiments [17]. The thermalized electrons from each flow provide a neutralizing background for the interpenetrating ions that drive the observed Weibel filamentation. This is characteristically different from astrophysical collisionless shocks, where Coulomb collisions are negligible, and poses a limitation in the comparison of plasma temperatures between laboratory and astrophysical collisionless shocks. However, due to the high collisionality of the electrons, characterization of the electron density and temperature provide an accurate description of the plasma within the midplane during the interaction in laboratory experiments.

III. SATURATION ANALYSIS USING BENCHMARKED FLASH SIMULATIONS

Temporally resolved TS measurements at the midplane for the 8mm cases are used to benchmark FLASH [35] calculations.[1] To compare with TS data, 2D FLASH calculations of a single foil are performed and the midplane electron density is doubled and corrected for the expected charge state[2] because single-foil simulations will calculate a much lower temperature than what is observed in the two-foil interactions [17]. Figure 2 shows temporally resolved measurements (data points) of n_e and plasma flow velocity ($V/2$), where the error

---

[1]Due to the configuration of the experiment, the flow velocity was not measurable in the 5 mm cases.

[2]An average charge state is estimated using measured T_e and n_e from TS data and assumed to be constant during the interaction with the following values: $<Z>_{\mathrm{CH8mm}}=3.5$; $<Z>_{\mathrm{Al8mm}}=11$; $<Z>_{\mathrm{Cu8mm}}=19$; $<Z>_{\mathrm{CH5mm}}=3.5$; $<Z>_{\mathrm{Al8mm}}=12$; $<Z>_{\mathrm{Cu5mm}}=20$.

bars are calculated for each point using an R^2 analysis based on how well the spectra are fitted.

Solid lines are the results from FLASH calculations using a 70% laser-absorption fraction and show good agreement for the temporal evolution of fluid velocity for all three materials. FLASH-calculated electron-densities also agree with TS measurements well for the CH and Al cases, but TS measurements are $\gtrsim 10$ times higher for the Cu cases. The most likely cause for this discrepancy is radiative effects that are not captured in the single-foil calculations due to low simulated T_e, but are present in the two-foil experiments.[3] Optically thin, radiative

---

[3]Two-foil simulations would assume that the interaction is purely collisional, which is not the case for the ions, and would over predict the density of the plasma.
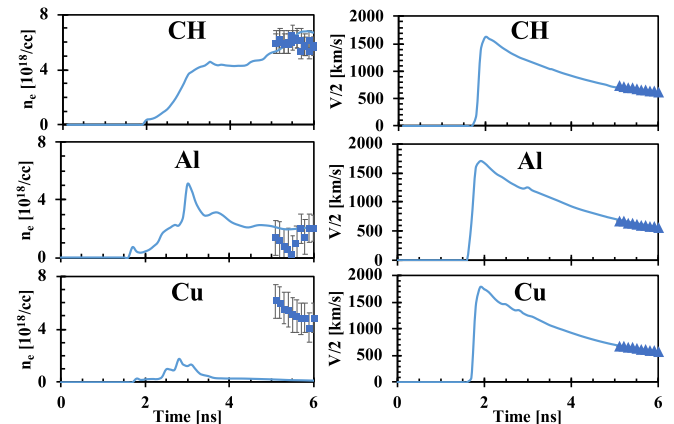

FIG. 2. Electron-density and fluid-velocity measurements at the midplane are shown for the 8 mm case of all three materials. Post-processed FLASH calculations agree well with experimental data for the plastic and aluminum cases. However, the measured density in the copper experiment is $\gtrsim 10$ times higher than FLASH calculations.

timescales τ_{thin} are $\sim 10^2$ ns, $\sim 10^1$ ns, and $\sim 10^{-2}$ ns for the CH, Al, and Cu cases, respectively. Copper will radiate energy away faster than the typical ~ 1 ns timescales relevant to Weibel growth, allowing higher electrons densities to be achieved in the experiments than predicted from overlapped single-foil calculations. The effect of this discrepancy will be discussed in Sec. V. Nonetheless, good agreements in the CH and Al cases suggests that utilizing FLASH calculations to estimate the temporal evolution of plasma conditions is warranted.

A saturation analysis is performed using the temporally evolving plasma conditions to demonstrate how application of the linear theory at different times changes the predicted Weibel-filament scale-size. Initially, small perturbations in the system will grow according to linear theory, but once amplitudes are too large and nonlinear growth of the system occurs, linear theory no longer applies. The linear growth rate $\Gamma(k)$ is calculated as a function of mode number ($k = 2\pi/\lambda$) using a dispersion relation that accounts for collisional electrons and intrastream ions, while allowing inter-stream ions to be collisionless [36]. Assuming symmetric flows at the midplane, FLASH-calculated densities and velocities are used at each time step, and the charge-state Z and plasma temperature T_e are approximated as constants. Additionally, it is assumed that $T_i = T_e$, using the measured T_e values from TS data [Fig. 1(c)].[4] The saturation wavelength Λ_{sat} is determined by the maximum of Γ^2/k at each time step since this determines the limit for magnetic trapping [13], e.g., the CH-8mm case at 2 and 3 ns as shown in Figs. 3(a) and 3(b). It is noted that Λ_{sat} ($\sim \lambda_W \sim \delta_i$) begins large due to the low-density (large δ_i) at the leading edge of the plasma plume, and reduces as the higher-density (small δ_i) material enters the midplane. The growth rate of the saturation mode (Γ_{sat}) for the CH-8 mm case is shown in Fig. 3(c) and show initial linear growth times to be ~ 300–500 ps and expected saturated B-field strengths of ~ 2–3 T.

The saturation analysis shows that there is expected variation in the dominant Weibel-filament size as a function of time. To account for this temporal variation, an average Weibel wavelength $< \Lambda_{sat} >$ is defined as the temporal average of Λ_{sat} over a defined duration. The results of these calculations are shown in Figs. 4(a) and 4(b) when averaging over the first linear growth time (~ 300–500 ps) and when averaging up to the proton timing, respectively. When averaging up to the proton time, higher plasma densities reduce the expected Weibel wavelength relative to the initial collisionless interaction. Using either metric, it is clear that the expected dominant mode is relatively unchanged when altering the material or separation distance between the two foils. However, for the copper cases, the measured densities later in time

---

[4]While the TS analysis provides a measurement of T_i in the 8 mm cases, additional complexities arise with the ion-feature form-factor for mid-Z ions (Al and Cu) to infer T_i; this is not an issue for the velocity measurement. The assumption of thermal equilibrium between electrons and ions is not necessarily warranted in all cases, however, the effect this has on the calculated scale size and saturated B-field strength of the ion-Weibel instability is small compared to the error bars already associated with those calculations.
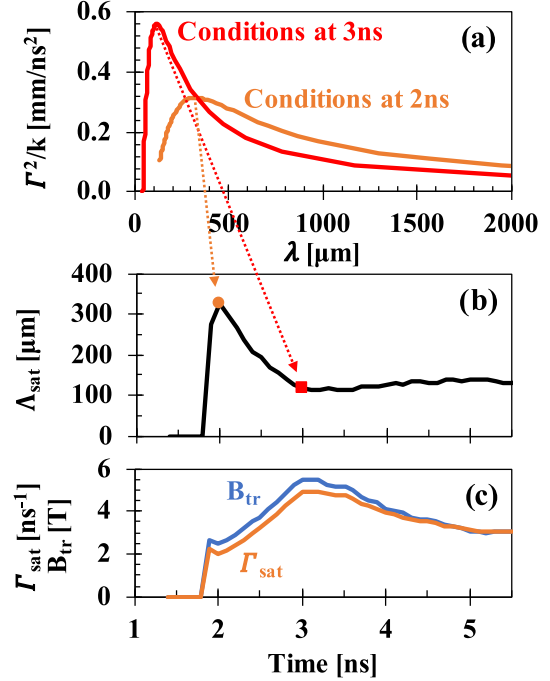

FIG. 3. Results from the saturation analysis of the CH-8 mm case utilizing benchmarked FLASH calculations. (a) Ion-Weibel growth rate Γ^2/k for the plasma conditions at the midplane at 2 ns (orange) and 3 ns (red). (b) Saturation wavelength (Λ_{sat}) as a function of time due to changing plasma conditions at the midplane. (c) Linear growth rate (Γ_{sat}) and saturated B-field strength (B_{tr}) at the saturation wavelength.

are $\gtrsim 10\times$ higher than FLASH calculations, though at early times the exact magnitude of this discrepancy is unknown. Radial variation of plasma conditions is expected to cause a similar effect since the density falls off with radius, such that a larger Λ_{sat} would be calculated at the edge of the plasma.

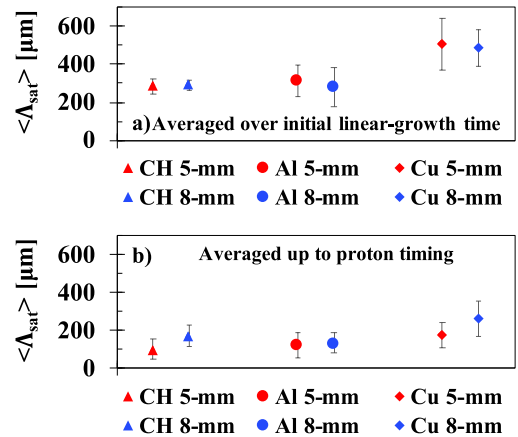FIG. 4. Results from the saturation analysis applied to benchmarked FLASH simulations when (a) averaging over the initial linear growth time (~ 300–500 ps), or (b) averaging over all values up to the proton time. Typical values in panel (b) are $\sim 40\%$ of the values in panel (a) due to higher plasma densities at later times. The vertical error bars are plus and minus one standard deviation for each case.

Uncertainties in Λ_{sat} due to radial plasma variation calculated in FLASH are predicted to be small at first and can reach levels of ±10–20% by ~400 ps after the initial interaction. Uncertainties shown in Fig. 4(a) due to axial plasma variation over the first linear growth time are also representative of this radial effect. The saturation analysis using benchmarked FLASH calculations provides insightful metrics from linear theory for each of the six cases to compare with measurements from proton images.

IV. FOURIER ANALYSIS OF PROTON IMAGES

A. Utilizing spectra of proton fluence

Proton images of the interaction region in these counter-streaming plasmas, as shown in Fig. 1(b), reveal complex electromagnetic-field structures in all six cases. The primary structures of interest to the ion-Weibel instability are the filaments that form along the flow direction with a wave vector that is transverse to the flow. Computational particle-in-cell (PIC) studies of similar systems [15] have shown that during the collisionless, ion-driven regime, electric fields due to the ion-Weibel instability are present, but with energy densities $\sim100\times$ smaller than those due to magnetic fields. For this reason, we assume that transverse deflections in proton images are due solely to magnetic fields generated by the "forest" of Weibel-driven ion-current filaments. The so-called "forest effect" has been statistically studied by Levesque *et al.* [33] to assess how the depth of the interaction region affects the inherently path-integrated sensitivity of proton imaging.

This statistical analysis shows that that the dominant mode found from Fourier analysis of proton images directly correlates with the filament size. This technique requires that proton trajectories not be altered by any other field structures and deflections by a single filament must be small. Given the imaging geometry used in this work, the deflections of 15 MeV protons are expected to be in this regime for azimuthal B fields around Weibel filaments of $\lesssim 50$ T [33].[5] We note here that deflections of protons by azimuthal B fields around Weibel filaments are dependent on the transverse component of the proton velocity, specifically the vertical velocity component in the coordinate system of Fig. 1(b) images. To utilize this analysis technique, no other B fields can affect proton trajectories, such as the horizontal void apparent in these proton images, and observed in other experiments [18,20,21]. Therefore, the Fourier analysis of proton filaments was conducted on each image in the region indicated by the gray box in Fig. 1(b).

The normalized mean-square spectrum (MSS) is calculated in the analysis region of each image and shown in Fig. 5 by the solid lines. Each spectrum is fit to the functional form

$$f(\lambda) = C\frac{e^{-(L/\lambda)^2}}{\lambda^2}, \tag{5}$$

where C is a normalization constant, and $L = \pi a$, where a is the representative radius of a current filament. This statistical
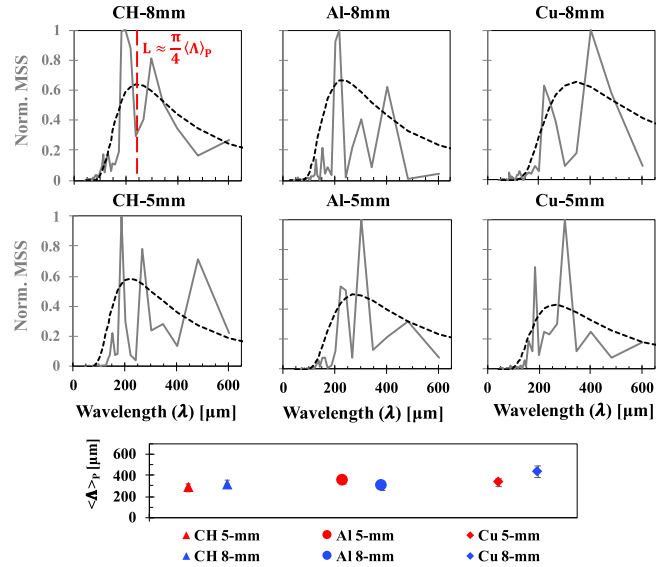

FIG. 5. Mean-square spectra (solid gray) are shown as a function of wavelength for each experimental case. The dominant Weibel wavelength inferred from proton data $\langle\Lambda\rangle_P$ is related to the characteristic length (L) of the functional fits (dashed black) to the spectra.

analysis of proton images provides a direct estimate of the dominant wavelength for filaments, assuming a random Gaussian field with characteristic length scale $L = \pi a$, where a is the radius of a representative filament. The Weibel wavelength inferred from proton images ($\langle\Lambda\rangle_P$) can be approximated by two filaments with opposite currents, such that $\langle\Lambda\rangle_P \sim (4/\pi)L$. Functional fits to each spectrum (short dashed lines) are shown for all cases and the results summarized in the bottom plot Fig. 5. Error bars are set at $\pm18\%$ due to the variability in magnification for a ~3 mm disk of filaments centered 10 mm from the proton source; this is larger than the statistical uncertainties of the fitting method. This analysis, however, does not provide an estimate of B-field size. To do this, proton images are deconvolved to provide path-integrated B-field (BL) distributions to asses scale sizes and estimate field strengths.

B. Utilizing spectra of path-integrated B fields

Proton images are analyzed in the linear-deflection regime using the iterative PROBLEM solver [37] code to retrieve BL distributions. Convergence of the iterative solver is reached when the range of the path-integrated values asymptotes, typically after $\sim400\,000$ iterations. Resulting BL distributions are shown in Fig. 6(a). These images were processed with a bandpass filter, keeping only wavelengths between ~40–$650\ \mu$m to illustrate features on the same color scale. The path-integrated B-field magnitudes in the analysis regions [gray boxes in Fig. 6(b)] are determined using the vertical component of the proton velocity at that location. Fourier analysis of BL lineouts quantifies the sinusoidal amplitude $<$BL$>$ of each mode present in the spectrum, as shown by the mean-square-spectra plots in Fig. 6(b). The $<$BL$>$ spectra (blue) typically show an MSS amplitude that increases with wavelength and falls off at the longest wavelengths.

---

[5]This assumption holds while the filaments are nearly straight in the flow direction, however, later in time, as longitudinal modes begin to grow, this assumption is no longer valid.
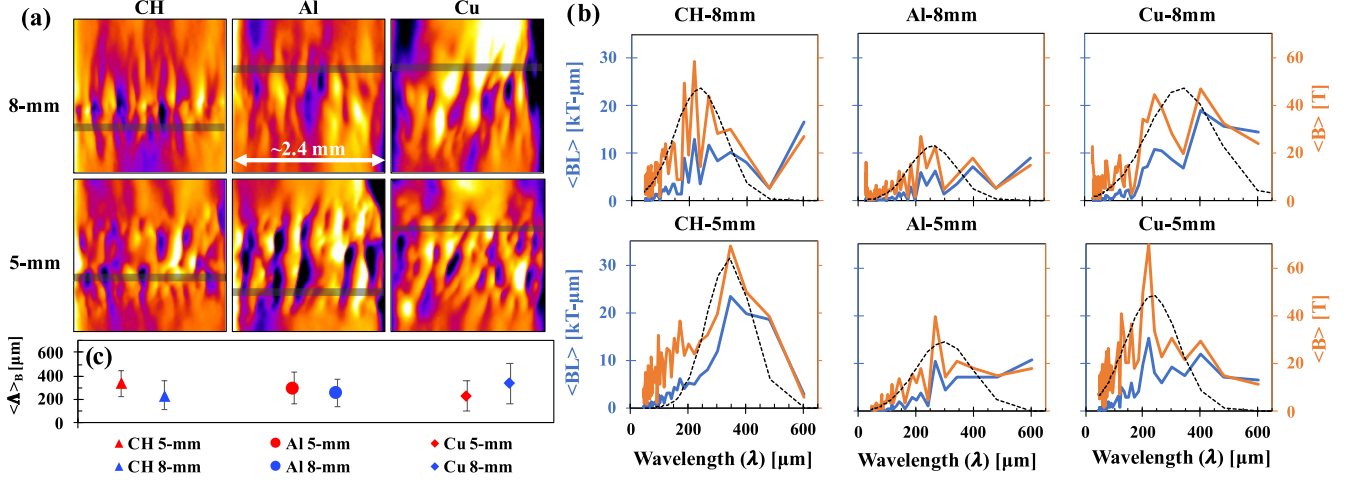
FIG. 6. (a) Path-integrated B-field distributions derived from normalized proton fluence images, showing only the B-field component from azimuthal fields surrounding current filaments. Boxed regions, 93 μm wide, are used for Fourier analysis. (b) Mean-square-spectra plots (blue) in the boxed regions, where <BL> is the sinusoidal amplitude at wavelength λ. To estimate the B-field amplitude <B>, the wavelength is used as the scale length and plotted (orange) as a function of wavelength. Note that the resolution of the proton backlighter is limited by its source size, FWHM $\sim$ 45 μm. (c) Average wavelength from <B> spectra ($\langle\Lambda\rangle_B$) with 1σ error bars determined by Gaussian fits in each case.

To help identify a band of dominant modes and estimate B-field amplitudes from <BL> spectra, the scale length is approximated as a scalar multiple of the wavelength, such that N<B>$\sim$<BL>$/\lambda$, where N is the number of wavelengths it takes to imprint an effective <BL> value on to the proton trajectory. Path-integrals of simulated proton trajectories by Levesque *et al.* [33] suggest that $N \sim$1–3 under similar imaging conditions.

The resultant <B> spectra (orange) are shown in Fig. 6(b), assuming $N = 1$. These spectra generally show a broad peak and are fit to a Gaussian (dashed) to provide a measure for the inferred Weibel wavelength $\langle\Lambda\rangle_B$ and its variance ($\pm$ one standard deviation), as well as an estimate of the sinusoidal B-field strength $\langle B\rangle_B$ based on the amplitude of the fit. The uncertainty in the B-field strength, separate from the scalar multiplier N, is based on the geometric variation of the vertical proton velocity across the analysis region; this is usually $\sim$30%. A summary of the inferred wavelengths and associated variances from this analysis is shown in Fig. 6(c). Results of these analyses are compared with values derived from the saturation analysis in the next section.

V. DISCUSSION

Dominant Weibel modes derived from proton images through Fourier analysis are shown to be consistent with saturation values calculated using plasma conditions from the initial collisionless interaction. Figure 7(a) shows the comparison between the dominant wavelength inferred from proton spectra (<Λ>$_P$) and the saturation wavelength (<Λ>$_{sat}$) using plasma conditions during the first linear growth time of the interaction [Fig. 4(a)] for all six cases. Measurements from proton data in the CH and Al cases lie near the <Λ>$_P$=<Λ>$_{sat}$ (dashed) line, suggesting that the Weibel evolution reached saturation and growth is in the nonlinear regime. Note, that if the saturation wavelength averaged up to the proton time [Fig. 4(b)] were used instead, that the points

would be shifted to the left by a factor of $\sim$2$\times$. We also note here that the copper cases (diamonds) lie to the right of the dashed line due to the low densities predicted by FLASH calculations due to radiative effects, as discussed in Sec. III. However, the effects of radiative cooling in the two-flow interaction will be small during the initial $\lesssim$ 500 ps, and we don't expect experimental densities to deviate from FLASH calculations as much at early times as the $\gtrsim$10$\times$ observed at later times. Using the dashed line as a guide, the FLASH-predicted Cu density may only be low by $\sim$2–3$\times$, and this discrepancy would grow in time due to accumulated radiative losses. We conclude from these results that the wavelengths of Weibel filaments derived from proton data are spectrally consistent with the saturation of the ion-Weibel instability using plasma conditions of the initial $\sim$300–500 ps of the collisionless interaction, though proton data are taken $\gtrsim$2 ns later in time.

The comparison between <Λ>$_B$ and <Λ>$_{sat}$> is shown in Fig. 7(b) and illustrates similar trends as <Λ>$_P$. This demonstrates consistency between the two analysis methods, and the B-field strength can now be estimated as the peak amplitude of the <B> spectrum. Figure 7(c) shows the inferred B-field strengths <B>$_B$ for each case assuming $N = 1$ and the sensitivity to the vertical proton velocity is evident by the large error bars. For $N = 1$, inferred <B>$_B$ values are an order of magnitude higher than the calculated saturation B-field strength <B$_{tr}$>. To bring these data in line with linear theory, Fig. 7(c) shows that Cu and CH data clump together along a line where $N \approx 22$ and the Al data clump around $N \approx 9$. Both of these values are high when compared with the expected value of $N \sim$1–3 derived from simulated trajectories through a forest of filaments [33]. Even with the additional uncertainty of $\sim$2$\times$ in the path length, inferred <B>$_B$ are still $\gtrsim$5–10$\times$ higher than the saturation value at the initial plasma conditions. This is likely due to the inhomogenous plasma profiles entering the interaction region.
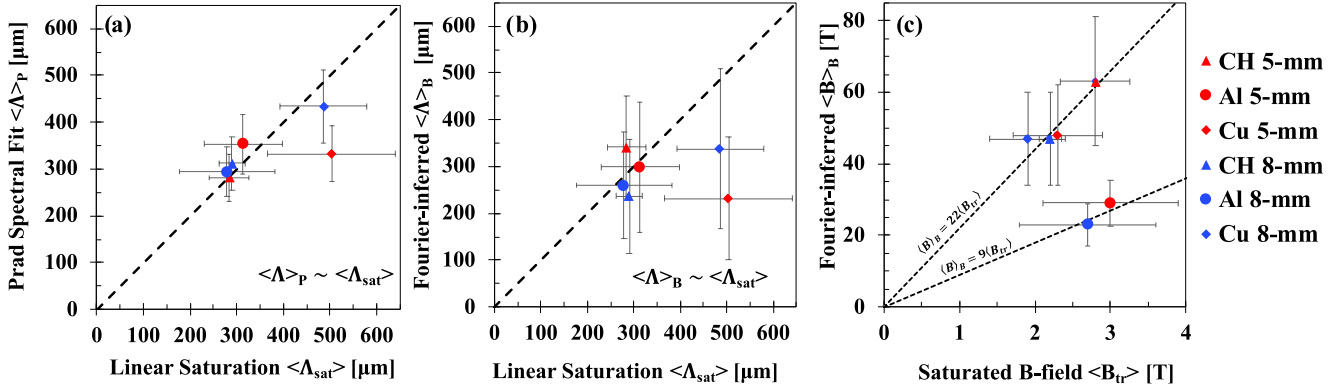
FIG. 7. Comparison of the estimated dominant wavelength from the saturation analysis $\langle \Lambda_{sat} \rangle$ with the inferred dominant wavelength determined from the Fourier analysis of (a) proton spectra $\langle \Lambda \rangle_P$ and (b) <B> spectra $\langle \Lambda \rangle_B$. (c) Comparison of the saturated B-field strength $\langle B_{tr} \rangle$ from the saturation analysis and the estimated B-field strength $\langle B \rangle_B$ inferred from Gaussian fits to <B> spectra.

Recent numerical work by Grassi *et al.* [29] studied the effects of plasma inhomogeneity on collisionless shock formation in counterstreaming flows using 2D PIC calculations. Analysis of the B fields at the midplane indicated that the evolution of the dominant magnetic wavelength was not greatly affected by an increasing plasma density. However, the increasing plasma density in simulations was shown to increase the B-field strength substantially ($\gtrsim$3–5$\times$) higher than the saturated value during nonlinear growth, whereas the homogenous simulations stayed relatively consistent with the linear theory throughout the nonlinear phase.[6] This was attributed to less effective Weibel growth away from the midplane and enhanced field advection towards the midplane due to the asymmetries introduced by the inhomogenous flows. While the plasma profiles simulated do not exactly match the experimental evolution, the expected effects are similar in that the B fields in the midplane are expected to quickly exceed the saturated value by factors of a few during nonlinear growth.[7] Fourier-inferred B-field amplitudes from proton data are consistent with continuous growth past the saturation limit, and assuming a path-length factor of $N \sim 2$, indicate B-field amplitudes of $\sim$25T for the CH and Cu cases and $\sim$12T for the Al cases. These values are significantly higher than predicted saturation levels by $\sim$10$\times$ and $\sim$5$\times$ for the CH/Cu and Al cases, respectively.

Weibel growth, as revealed by proton images, is in its nonlinear phase for all cases discussed. Analyses of these images show that the dominant magnetic wavelength inferred from proton data is consistent with the saturation wavelength based on initial plasma conditions of the collisionless interaction. Furthermore, the inferred B-field strength, despite the

factor-few uncertainty, still indicates that the B fields are significantly stronger than the saturation value, consistent with 2D PIC calculations of similar inhomogenous flows. Given a typical linear growth time of $\sim$400 ps and the timing of proton images, observed filaments have evolved for $\sim$5–6 linear growth times. However, the dominant magnetic wavelengths are still consistent with the linear value, suggesting that filament merging happens later in time under these conditions.

Figure 8(a) shows normalized proton images at four different times for the CH-5 mm case, illustrating the nonlinear evolution of Weibel filaments. These images are Fourier analyzed in the same way as discussed in Sec. IV, with spectra from proton images and corresponding BL-distributions shown in Figs. 8(b) and 8(c), respectively. The inferred dominant wavelengths, $<\Lambda>_P$ (black squares) and $<\Lambda>_B$ (orange circles), from these analyses are shown in Fig. 8(d) and are consistent until the 5.5 ns image. It is evident from these spectra, that at later times, the filaments are larger in size and that the inferred B field grows in time. The exception to that trend is in the last image, where $<B>_B$ and $<\Lambda>_B$ seem to be slightly lower. This is likely due to the inaccuracy of the inversion of the proton data.

The 5.5 ns image in Fig. 8(a) shows the emergence of caustic behavior, invalidating the linear assumption inherent in the deconvolution method used. However, the gradual appearance of caustics still indicates the continued growth of the B-field strength further into the nonlinear regime and the Fourier analysis can still provide a useful estimate of scale size given typical uncertainties. The localized transfer of magnetic energy from small to large scales is consistent with the coalescence of Weibel-driven current filaments. Assuming constant plasma parameters, a nonlinear coalescence model [15] is applied to the first $\sim$400 ps of the interaction, indicating a slow increase of the dominant Weibel wavelength as shown by the dashed gray lines in Fig. 8(d). This nonlinear coalescence model [15] also suggests that, for these plasma conditions, the dominant Weibel wavelength stays near $<\Lambda_{sat}>$ for multiple nanoseconds, consistent with the experimental observation that the dominant wavelength in the nonlinear regime was the same as the saturation wavelength based on initial plasma conditions. In contrast to the plasma conditions found in these Omega experiments, the faster, denser systems achievable at

---

[6]In Fig. 2(b) of Ref. [29] the ion gyroradius for the inhomogenous case is shown to continuously decrease during nonlinear growth despite the decreasing velocity profile, indicating an increasing B-field strength during this time.

[7]It is important to note here that even though the analysis of BL images was performed away from the exact midplane, we expect similar evolutionary behavior as the 'exact' midplane since the leading edge of each flow travels $\sim$600–700μm in a linear growth time ($\sim$400 ps) and this is larger than the offset used in analyzing BL images.
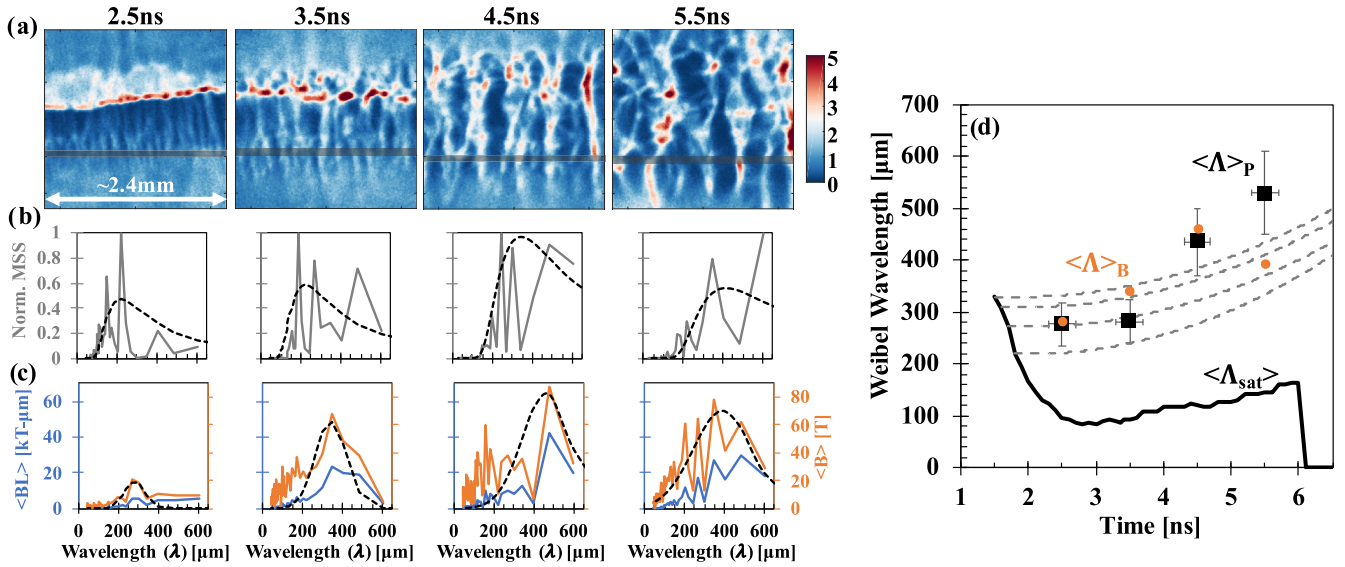
FIG. 8. Time evolution data taken of the CH-5mm configuration. Normalized proton images are shown in panel (a) with the analysis regions indicated. Spectra from proton data are shown in panel (b), spectra from BL distributions are shown in panel (c). The dominant wavelength as determined from proton spectra $<\Lambda>_P$ (black squares) and BL spectra $<\Lambda>_B$ (orange circles) are shown as a function of time in panel (d). The temporal evolution of the saturation analysis based on FLASH simulations is plotted (solid black) for comparison with data. A nonlinear coalescence model [15] is applied to the first $\sim$400 ps of the interaction, assuming constant plasma conditions, and are shown (dashed gray) to represent the trend in the data well.

the NIF [27] saturate earlier and filaments coalesce faster, resulting in turbulent B-field amplification and shock formation during the experiment.

VI. SUMMARY

Weibel-driven magnetic fields are robustly produced under varying plasma conditions in counterstreaming plasmas of CH, Al, and Cu and clearly observed in 15 MeV proton images. FLASH simulations of the collisionless interaction at the midplane are benchmarked with Thomson scattering measurements to estimate plasma parameters at all times during the experiment. A saturation analysis using benchmarked plasma parameters from FLASH show that typical linear-growth times during the initial plasma conditions ($V \sim$1600–2000 km/s, $n_e \sim 5 \times 10^{17}$ cm^{-3}) are $\sim$300–500 ps, suggesting that Weibel instability growth reaches saturation at a scale-size ($<\Lambda_{sat}>$) based on the magnetic trapping criterion [11–14] before B fields are detectable using proton radiography. Dominant wavelengths are inferred later in time from data through a Fourier analysis of proton fluence images ($<\Lambda>_P$) and corresponding BL distributions [37] ($<\Lambda>_B$). These values are consistent with each other and with $<\Lambda_{sat}>$ for the CH and Al cases at both 5 and 8 mm, with a dominant wavelength of $\sim$300 μm. The saturated wavelength for Cu cases suggest slightly higher densities than predicted by FLASH, which could be due to radiative effects not captured in collisionless FLASH estimates or radiation effects on the linear and nonlinear evolution of Weibel filaments. Despite the large uncertainties on B-field estimates from proton images, the inferred B-field strengths suggest continued growth of the B field into the nonlinear regime resulting in $\sim$25T and $\sim$12T amplitudes for the CH/Cu and Al cases, respectively. This result is consistent with recent numerical work by Grassi

et al. [29] which showed a significant enhancement in B-field growth after saturation due to an increasing plasma density, whereas calculations with homogenous plasma profiles suggested a nearly constant B-field strength well into the nonlinear phase.

The level of spectral analysis presented here surpasses all previous works using this experimental platform. At this level of detail, we can experimentally demonstrate that the initial collisionless interaction of the two flows sets the spectral characteristics of the Weibel evolution and that linear analysis of the plasma at later times will be inaccurate since the system is already in the nonlinear regime. We also demonstrate that the temporal evolution of Weibel-filament scale-size in the CH-5 mm case is consistent with a nonlinear filament-coalescence model [15] applied to plasma conditions during the initial collisionless interaction. Spectra inferred from proton data clearly show the transfer of magnetic energy in time from small to large spatial scales, though direct quantification of this is difficult given the uncertainties in the measurement. During the times probed in the CH-5 mm case, the results suggest a single-coalescence of the saturation wavelength of $\sim$300 μm; an observation made possible by the detailed Fourier analysis of deconvolved proton images. With these new analysis techniques in mind, future experiments are being designed and executed to study the effects that an external B field has on ion-Weibel filamentation because many astrophysical collisionless shocks are formed in the presence of a background magnetic field.

[1] K. Koyama, R. Petre, E. V. Gotthelf, U. Hwang, M. Matsuura, M. Ozaki, and S. S. Holt, Nature (London) **378**, 255 (1995).

[2] M. Ackermann, M. Ajello, A. Allafort, L. Baldini, J. Ballet, G. Barbiellini, M. G. Baring, D. Bastieri, K. Bechtol, R. Bellazzini, R. D. Blandford, E. D. Bloom, E. Bonamente, A. W. Borgland, E. Bottacini, T. J. Brandt, J. Bregeon, M. Brigida, P. Bruel, R. Buehler *et al.*, Science **339**, 807 (2013).

[3] A. R. Bell, Mon. Not. R. Astron. Soc. **182**, 147 (1978).

[4] R. D. Blandford and J. P. Ostriker, Astrophys. J. **221**, L29 (1978).

[5] A. Spitkovsky, Astrophys. J. Lett. **682**, L5 (2008).

[6] H. J. Völk, E. G. Berezhko, and L. T. Ksenofontov, Astron. Astrophys. **433**, 229 (2005).

[7] E. S. Weibel, Phys. Rev. Lett. **2**, 83 (1959).

[8] B. D. Fried, Phys. Fluids **2**, 337 (1959).

[9] T. N. Kato and H. Takabe, Astrophys. J. **681**, L93 (2008).

[10] A. M. Taylor, I. Vovk, and A. Neronov, Astron. Astrophys. **529**, A144 (2011).

[11] R. C. Davidson, D. A. Hammer, I. Haber, and C. E. Wagner, Phys. Fluids **15**, 317 (1972).

[12] T. B. Yang, J. Arons, and a. B. Langdon, Phys. Plasmas **1**, 3059 (1994).

[13] A. Achterberg, J. Wiersma, and C. A. Norman, Astron. Astrophys. **475**, 19 (2007).

[14] C. Ruyer, L. Gremillet, G. Bonnaud, and C. Riconda, Phys. Rev. Lett. **117**, 065001 (2016).

[15] C. Ruyer, L. Gremillet, A. Debayle, and G. Bonnaud, Phys. Plasmas **22**, 032102 (2015).

[16] Y. Kuramitsu, Y. Sakawa, T. Morita, C. D. Gregory, J. N. Waugh, S. Dono, H. Aoki, H. Tanji, M. Koenig, N. Woolsey, and H. Takabe, Phys. Rev. Lett. **106**, 175002 (2011).

[17] J. S. Ross, S. H. Glenzer, P. Amendt, R. Berger, L. Divol, N. L. Kugland, O. L. Landen, C. Plechaty, B. Remington, D. Ryutov, W. Rozmus, D. H. Froula, G. Fiksel, C. Sorce, Y. Kuramitsu, T. Morita, Y. Sakawa, H. Takabe, R. P. Drake, M. Grosskopf *et al.*, Phys. Plasmas **19**, 056501 (2012).

[18] H. S. Park, C. M. Huntington, F. Fiuza, R. P. Drake, D. H. Froula, G. Gregori, M. Koenig, N. L. Kugland, C. C. Kuranz, D. Q. Lamb, M. C. Levy, C. K. Li, J. Meinecke, T. Morita, R. D. Petrasso, B. B. Pollock, B. A. Remington, H. G. Rinderknecht, M. Rosenberg, J. S. Ross *et al.*, Phys. Plasmas **22**, 056311 (2015).

[19] D. B. Schaeffer, E. T. Everson, A. S. Bondarenko, S. E. Clark, C. G. Constantin, D. Winske, W. Gekelman, and C. Niemann, Phys. Plasmas **22**, 113101 (2015).

[20] C. M. Huntington, F. Fiuza, J. S. Ross, A. B. Zylstra, R. P. Drake, D. H. Froula, G. Gregori, N. L. Kugland, C. C. Kuranz, M. C. Levy, C. K. Li, J. Meinecke, T. Morita, R. Petrasso, C. Plechaty, B. A. Remington, D. D. Ryutov, Y. Sakawa, A. Spitkovsky, H. Takabe *et al.*, Nat. Phys. **11**, 173 (2015).

[21] C. M. Huntington, M. J.-E. Manuel, J. S. Ross, S. C. Wilks, F. Fiuza, H. G. Rinderknecht, H.-S. Park, G. Gregori, D. P. Higginson, J. Park, B. B. Pollock, B. A. Remington, D. D. Ryutov, C. Ruyer, Y. Sakawa, H. Sio, A. Spitkovsky, G. F. Swadling, H. Takabe, and A. B. Zylstra, Phys. Plasmas **24**, 041410 (2017).

[22] D. B. Schaeffer, W. Fox, D. Haberberger, G. Fiksel, A. Bhattacharjee, D. H. Barnak, S. X. Hu, and K. Germaschewski, Phys. Rev. Lett. **119**, 025001 (2017).

[23] W. Fox, J. Matteucci, C. Moissard, D. B. Schaeffer, A. Bhattacharjee, K. Germaschewski, and S. X. Hu, Phys. Plasmas **25**, 102106 (2018).

[24] D. B. Schaeffer, W. Fox, R. K. Follett, G. Fiksel, C. K. Li, J. Matteucci, A. Bhattacharjee, and K. Germaschewski, Phys. Rev. Lett. **122**, 245001 (2019).

[25] G. F. Swadling, C. Bruulsema, F. Fiuza, D. P. Higginson, C. M. Huntington, H. S. Park, B. B. Pollock, W. Rozmus, H. G. Rinderknecht, J. Katz, A. Birkel, and J. S. Ross, Phys. Rev. Lett. **124**, 215001 (2020).

[26] P. V. Heuer, M. S. Weidl, R. S. Dorst, D. B. Schaeffer, S. K. P. Tripathi, S. Vincena, C. G. Constantin, C. Niemann, and D. Winske, Phys. Plasmas **27**, 042103 (2020).

[27] F. Fiuza, G. F. Swadling, A. Grassi, H. G. Rinderknecht, D. P. Higginson, D. D. Ryutov, C. Bruulsema, R. P. Drake, S. Funk, S. Glenzer, G. Gregori, C. K. Li, B. B. Pollock, B. A. Remington, J. S. Ross, W. Rozmus, Y. Sakawa, A. Spitkovsky, S. Wilks, and H. S. Park, Nat. Phys. **16**, 916 (2020).

[28] M. J.-E. Manuel, A. B. Zylstra, H. G. Rinderknecht, D. T. Casey, M. J. Rosenberg, N. Sinenian, C. K. Li, J. A. Frenje, F. H. Séguin, and R. D. Petrasso, Rev. Sci. Instrum. **83**, 063506 (2012).

[29] A. Grassi and F. Fiuza, Phys. Rev. Res. **3**, 023124 (2021).

[30] T. R. Boehly, V. N. Goncharov, O. Gotchev, J. P. Knauer, D. D. Meyerhofer, D. Oron, S. P. Regan, Y. Srebro, W. Seka, D. Shvarts, S. Skupsky, and V. A. Smalyuk, Phys. Plasmas **8**, 2331 (2001).

[31] J. R. Rygg, F. H. Seguin, C. K. Li, J. A. Frenje, M. J.-E. Manuel, R. D. Petrasso, R. Betti, J. A. Delettrez, O. V. Gotchev, J. P. Knauer, D. D. Meyerhofer, F. J. Marshall, C. Stoeckl, and W. Theobald, Science **319**, 1223 (2008).

[32] D. D. Ryutov, N. L. Kugland, M. C. Levy, C. Plechaty, J. S. Ross, and H. S. Park, Phys. Plasmas **20**, 032703 (2013).

[33] J. Levesque, C. C. Kuranz, T. A. Handy, M. J.-E. Manuel, and F. Fiuza, Phys. Plasmas **26**, 102303 (2019).

[34] D. D. Ryutov, N. L. Kugland, H. S. Park, C. Plechaty, B. A. Remington, and J. S. Ross, Phys. Plasmas **19**, 074501 (2012).

[35] P. Tzeferacos, M. Fatenejad, N. Flocke, C. Graziani, G. Gregori, D. Q. Lamb, D. Lee, J. Meinecke, A. Scopatz, and K. Weide, High Energy Density Phys. **17**, 24 (2015).

[36] D. D. Ryutov, F. Fiuza, C. M. Huntington, J. S. Ross, and H.-S. Park, Phys. Plasmas **21**, 032701 (2014).

[37] A. F. A. Bott, C. Graziani, P. Tzeferacos, T. G. White, D. Q. Lamb, G. Gregori, and A. A. Schekochihin, J. Plasma Phys. **83**, 905830614 (2017).